ADVANCED MATERIALS
www.advmat.de

Enhancing Efficiency of Low-Grade Heat Harvesting by Structural Vibration Entropy in Thermally Regenerative Electrochemical Cycles

Ahreum Choi, You-Yeob Song, Juyoung Kim, Donghyeon Kim, Min-Ho Kim, Seok Woo Lee, Dong-Hwa Seo,* and Hyun-Wook Lee**

The majority of waste-heat energy exists in the form of low-grade heat (<100 °C), which is immensely difficult to convert into usable energy using conventional energy-harvesting systems. Thermally regenerative electrochemical cycles (TREC), which integrate battery and thermal-energy-harvesting functionalities, are considered an attractive system for low-grade heat harvesting. Herein, the role of structural vibration modes in enhancing the efficacy of TREC systems is investigated. How changes in bonding covalency, influenced by the number of structural water molecules, impact the vibration modes is analyzed. It is discovered that even small amounts of water molecules can induce the A_{1g} stretching mode of cyanide ligands with strong structural vibration energy, which significantly contributes to a larger temperature coefficient (α) in a TREC system. Leveraging these insights, a highly efficient TREC system using a sodium-ion-based aqueous electrolyte is designed and implemented. This study provides valuable insights into the potential of TREC systems, offering a deeper understanding of the intrinsic properties of Prussian Blue analogs regulated by structural vibration modes. These insights open up new possibilities for enhancing the energy-harvesting capabilities of TREC systems.

1. Introduction

With the continued depletion of fossil fuels, increasing attention is being focused on energy-conversion systems that can effectively utilize waste energy against energy consumption.[1–3] The majority of waste energy is low-grade waste heat below 100 °C difference.[4,5] However, low-grade heat energy is rarely converted into usable energy using existing energy-harvesting systems because of the small temperature difference.[6,7] The thermally regenerative electrochemical cycle (TREC), which combines a battery and thermal energy-harvesting system, is capable of converting low-grade heat (<100 °C) into electrochemical energy.[3,8] In a battery system, some energy loss always occurs due to the various overpotentials[9] (η, such as the activation overpotential, ohmic overpotential, and concentration overpotential) (**Figure 1**a, left). However, these overpotentials can be overcome by designing the temperature coefficient (α) of each electrode material in a TREC system, and low-grade waste heat can be converted into usable electrochemical energy as shown in Figure 1a (right).

The temperature coefficient $\boldsymbol{\alpha}$ is the most critical variable for a high-performance TREC system:

$$\alpha = \frac{dV}{dT} = \frac{\Delta S}{nF} \tag{1}$$

where dV is the voltage difference, dT is the temperature difference, ΔS is the entropy change, n is the number of electrons transferred in the reaction, and F is Faraday's constant.[8] In particular, the sign of the temperature coefficient is important when designing a TREC. With a negative temperature coefficient, the charge voltage decreases at higher temperatures and the discharge voltage increases at lower temperatures, and vice versa. As the temperature coefficient is directly proportional to the entropy change, the amount of harvested work is significantly affected by its value (Figure 1b). Therefore, to design electrode materials with a high-temperature coefficient that can harvest more energy, it is necessary to consider the factors that affect the entropy change, as identified in previous studies:[10]

$$\Delta S = \Delta S_{ion} + \Delta S_{phn} + \Delta S_{conf} + \Delta S_{e^-} + \Delta S_{other} \tag{2}$$

A. Choi, Y.-Y. Song, J. Kim, D. Kim, M.-H. Kim, D.-H. Seo, H.-W. Lee
School of Energy and Chemical Engineering
Ulsan National Institute of Science and Technology (UNIST)
Ulsan 44919, Republic of Korea
E-mail: dseo@unist.ac.kr; hyunwooklee@unist.ac.kr

S. W. Lee
School of Electrical and Electronic Engineering
Nanyang Technological University
Singapore 639798, Singapore
E-mail: sw.lee@ntu.edu.sg

The ORCID identification number(s) for the author(s) of this article can be found under https://doi.org/10.1002/adma.202303199

DOI: 10.1002/adma.202303199

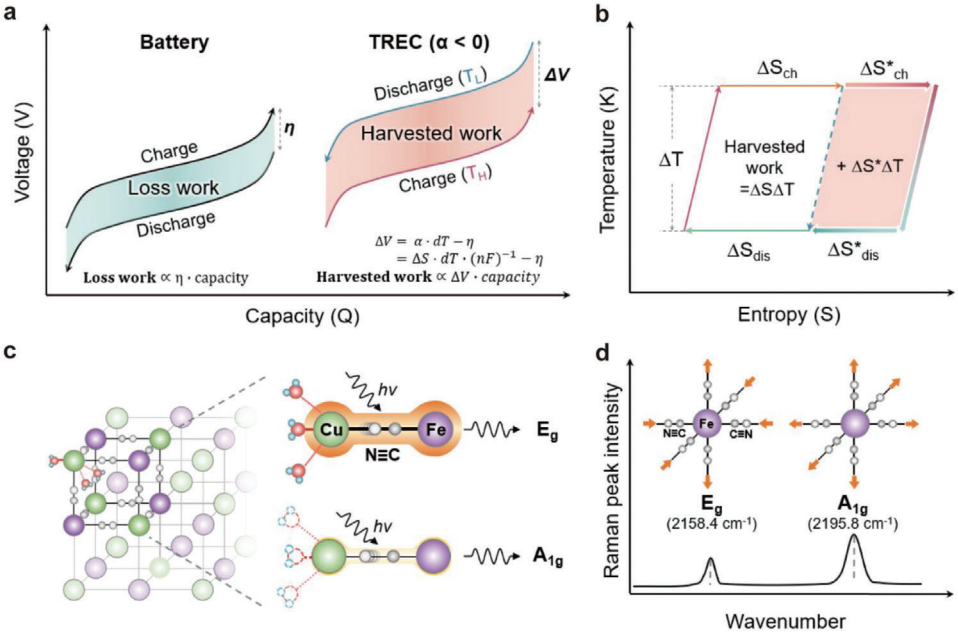

Figure 1. Principle of TREC and effect of water molecules in a PBA structure. a) Schematic showing the different mechanisms of a battery and TREC system. Whereas the battery system (left) loses some of the stored energy as unusable energy, the TREC system (right) can convert low-grade waste-heat energy into electrochemical energy during battery cycling. b) The amount of harvested work is determined from changes in entropy and temperature. To harvest a larger amount of work, the electrodes must undergo larger entropy changes during cycling. c) Effect of water molecules on the stretching vibration mode of cyanide ligands. d) Representative Raman spectra showing the vibration modes of E_g and A_{1g} of the PBA structure.

where ΔS_{ion} is the ion entropy, ΔS_{phn} is the phonon vibration entropy, ΔS_{conf} is the configuration entropy, ΔS_{e-} is the electron entropy, and ΔS_{other} is related to other factors that affect the electrochemical reaction. A comprehensive examination of these entropy changes in electrode materials is required to understand the underlying principles responsible for enhancing the performance of TREC systems.

Prussian blue analogs (PBAs) $P[R(CN)_6]$ where P is an N-coordinated transition metal and R is a C-coordinated transition metal) have been identified as representative and well-suited active materials for TREC systems.[8,10–12] The redox reaction of PBAs occurs within the stable voltage range of aqueous electrolytes applied in TREC systems.[13] In addition, the large channel size of PBAs reduces hysteresis during cation intercalation with a low degree of dehydration. There are two types of water molecules in the PBA structure: coordinated and interstitial water molecules. Coordinated water molecules are typically bonded to the N-coordinated transition metal via $R(CN)_6$ vacancies to compensate for charge valence, whereas interstitial water molecules are located in the empty channels of PBAs.[14] Although it is difficult to remove coordinated water molecules, as they are an integral part of the PBA structure, interstitial water molecules can move easily with charge carriers.

The present study highlights the impact of structural vibration entropy on copper hexacyanoferrate (CuHCFe) as a function of the number of water molecules, thereby contributing to the achievement of high-temperature coefficients.[8,10,11] According to our previous research,[11] the hydration entropy change with different hydration states of cations was associated with the number of water molecules present on the surface of cations. This effect could enhance the temperature coefficient value of −1.002 mV K^{-1} using Rb^+ cations. However, the hydration shells were almost inevitable to control due to their dependence on the cations employed. In addition, the deployment of electrolyte systems that rely on larger cations like Rb^+ may incur significant expenses and present logistical challenges for broad-scale implementation. Therefore, it is imperative to investigate additional influential factors inherent in the electrode materials, suggesting that the utilization of Na^+-ion electrolyte systems appears to be a viable approach for practical implementation, necessitating the identification of significant parameters within the electrode materials. The structural vibration entropy is considered a highly influential variable parameter. For example, interstitial water molecules surrounding the transition-metal ions can enhance the effect of coordinated water as shown in Figure 1c, leading to different directions of cyanide ligand stretching, E_g and A_{1g} (Figure 1d).[15–17] We have found the relationship between the covalency and symmetry of bonding strength in Raman spectra of the PBA structure by comparing different structural vibration modes. The covalency of Fe—C bonding is reduced in the presence of a lower quantity of water molecules, resulting in greater symmetry of the 6 Fe—C bonds compared to a higher quantity of water molecules. The structural vibration entropy triggers strong A_{1g} vibration modes in PBA, which entail strong vibration energy than the E_g vibration mode that is activated by water molecules. The different degrees of each structural vibration mode can affect the phonon vibration entropy change (ΔS_{phn}), which is closely related to structural vibration.[18] Therefore, the different bonding covalency between the transition metal and cyanide ligand, resulting in enhanced specific structural vibration modes, is intimately related to the temperature coefficient. Consequently, CuHCFe with a low amount of water molecules

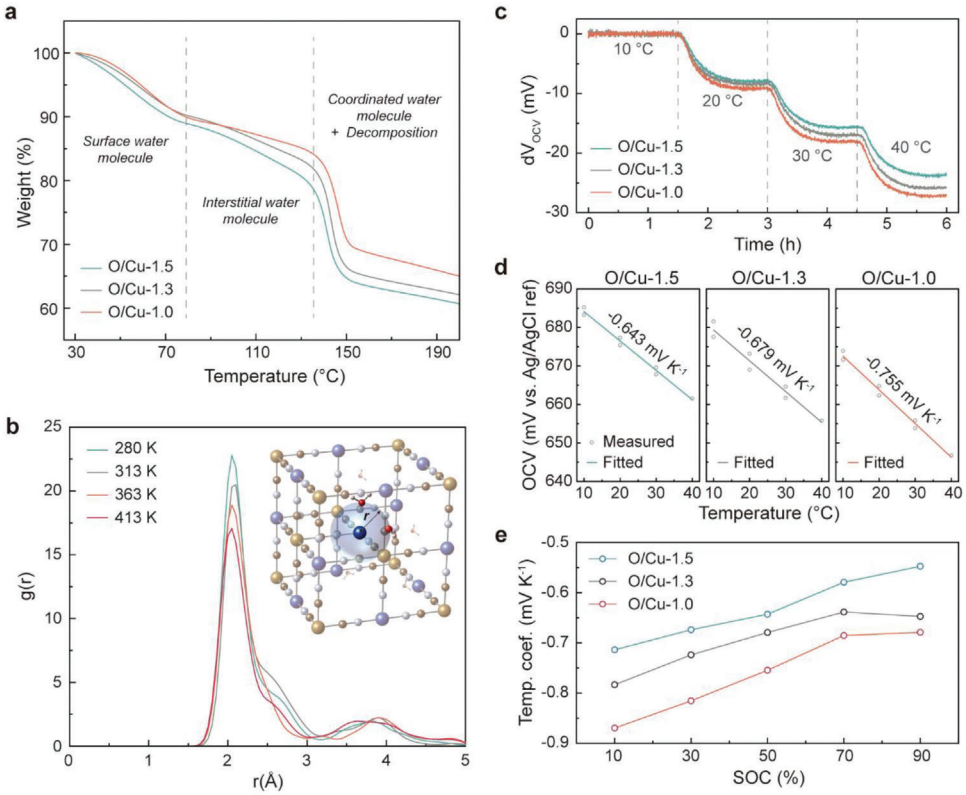

Figure 2. Effect of water molecules on temperature coefficient. a) TGA under an inert (N_2) atmosphere for three different CuHCFe samples, O/Cu-1.5, O/Cu-1.3, and O/Cu-1.0, containing varying amounts of water molecules. The heating rate was 1 °C min^{-1}. b) Partial radial distribution functions, g(r), for copper (coordinated by three CN groups) and oxygen of water within the CuHCFe structures, obtained from ab initio molecular dynamics simulations conducted at different temperatures. The peak near 2 Å in g(r) corresponds to the oxygen ion of coordinated water. c) The OCV changes of O/Cu-1.5, O/Cu-1.3, and O/Cu-1.0 at SOC 50% over the temperature range of 10–40 °C. d) Fitted data of OCV change used to calculate the temperature coefficients. e) Temperature coefficient of O/Cu-1.5, O/Cu-1.3, and O/Cu-1.0 from SOC 10% to SOC 90%. The temperature range of the measurements is the same as in that of (a).

can be applied in a high-efficiency TREC with a sodium-ion-based aqueous electrolyte (≈5% without a heat recuperation system).

2. Results

2.1. Temperature Coefficients of CuHCFe with Different Amounts of Water Molecules

To investigate the effect of interstitial and coordinated water molecules on CuHCFe, we prepared three different types of compound containing different amounts of water molecules. It is well known that three types of water molecules are related to the PBA structure:[19] surface water, interstitial water, and coordinated water. Surface water is located at the particle surface, whereas interstitial and coordinated water occupy empty spaces within the crystal structure. Coordinated water is bonded to exposed transition metals at vacancies, whereas interstitial water is found in the interstitial sites where sodium ions are inserted. To estimate the amounts of interstitial water, we employed thermogravimetric analysis (TGA). As observed in the TGA data in **Figure 2**a, there are three distinct temperature ranges: i) from room temperature to 75 °C, ii) from 75 to 140 °C, and iii) temperatures above 140 °C. According to previous work, HCN is detected when the temperature reaches the highest range (iii), indicating the thermal degradation of the structure by the decomposition of the cyanide ligand with coordinated water.[20] Otherwise, the loosely bonded water molecules evaporate at lower temperatures (i), indicating the presence of absorbed water molecules at the surface of CuHCF. As a result, the amount of interstitial water was calculated within range (ii). Based on the TGA and inductively coupled plasma-mass spectrometry (ICP-MS), we calculated the chemical formulas of O/Cu-1.5, O/Cu-1.3, and O/Cu-1.0 (Table S1, Supporting Information), which indicated that the samples had similar crystallinity but contained different amounts of interstitial water. To investigate the effect of the synthesis temperature on the water molecules within the PBA structure, we conducted ab initio molecular dynamics (AIMD) simulations at various temperatures (280, 313, 363, and 413 K). The analysis of the partial radial distribution functions (pRDFs, g(r)) for copper (coordinated by three CN groups) and oxygen of the water molecules in the structures is presented in Figure 2b. The pRDF analysis revealed that the intensity of the first peak decreased with increasing simulation temperature, suggesting reduced coordinated water molecules at high temperatures, which agrees with our experimental observations.

First, the temperature coefficients were determined by measuring the change in the open-circuit voltage (OCV) over a range of temperatures. As shown in Figure 2c,d, the OCV decreased with increasing temperature, indicating that CuHCFe has a negative temperature coefficient ($\alpha < 0$), which is consistent with previous research.[11] The temperature coefficients at the state of charge (SOC) 50% for O/Cu-1.5, O/Cu-1.3, and O/Cu-1.0 were −0.643, −0.679, and −0.755 mV K^{-1}, respectively, with O/Cu-1.0 showing a 17.4% and 11.2% improvement over O/Cu-1.5 and O/Cu-1.3, respectively. This trend was maintained throughout the entire range of SOC (Figure 2e). For example, the temperature coefficient of O/Cu-1.5 at SOC 10 and SOC 90 was −0.714 and −0.547 mV K^{-1}, respectively, while that of O/Cu-1.0 was −0.870 and −0.679 mV K^{-1}, representing improvements of 21.8% and 24.1% compared to O/Cu-1.5 at SOC 10% and SOC 90%, respectively. In addition, the temperature coefficient tends to increase as SOC decreases across the entire SOC range. Based on these trends, we can identify the two major influences on the temperature coefficient: i) when more sodium ions are intercalated in PBAs, the temperature coefficient rises, and ii) small amounts of water molecules can improve the temperature coefficient. The first effect may stem from the decreased lattice parameter resulting from the reduction of Fe(III) to Fe(II)[13] (Figures S1,S2, Table S2, Supporting Information). Thus, the effect of water molecules on the temperature coefficient will be the focus of our investigation.

2.2. Effectiveness of TREC Half-Cell

We operated the TREC half-cell using O/Cu-1.5, which has the lowest temperature coefficient, and O/Cu-1.0, which has the highest temperature coefficient, to compare the amount of harvested work and TREC cycle efficiency. As CuHCFe has a negative temperature coefficient, the TREC cell should be charged at high temperatures for lower operating potential and discharged at low temperatures for higher operating potential (**Figure 3**a). During the rest step between the charging and discharging processes, the OCV was evaluated to track the potential change. The closed-loop TREC in Figure 3b demonstrates that the discharge potential is higher than the charge potential in both TREC systems with O/Cu-1.5 and O/Cu-1.0, indicating that the TRECs effectively transformed heat energy into electrochemical energy in the battery system. We evaluated the performance of the TREC cell at various current densities and temperatures. First, the TREC cell was operated at temperature differences (ΔT) of 50 °C (from 10 to 60 °C), 40 °C (from 15 to 55 °C), and 30 °C (from 20 to 50 °C) with 0.5 C (30 mA g^{-1}) (Figure 3c).

The amount of harvested work W can be calculated using the following equation:

$$W = Q_{dis}\,V_{dis} - Q_{ch}\,V_{ch} = Q_{dis}\left(V_{dis} - \frac{V_{dis}}{CE}\right) \tag{3}$$

where Q_{dis} is the discharge capacity, Q_{ch} is the charge capacity, V_{dis} is the discharge voltage, V_{ch} is the charge voltage, and CE is the coulombic efficiency.[10] The amount of harvested work tends to decrease with decreasing temperature difference because there is less available heat energy to be converted into electrochemical energy after surmounting the energy loss by the overpotential. The average amount of harvested work for 20 cycles is 3.28 J g^{-1} (ΔT = 50 °C), 2.88 J g^{-1} (ΔT = 40 °C), and 1.24 J g^{-1} (ΔT = 30 °C) for O/Cu-1.0, and 2.64, 1.99, and 0.45 J g^{-1}, respectively, for O/Cu-1.5, indicating that more work can be produced for O/Cu-1.0 as expected.

The efficiency of heat-to-electricity conversion can be calculated using the following equation:

$$\eta = \frac{W}{T_H \Delta S + Q_{HR}} = \frac{W_{discharge} - W_{charge}}{|\alpha|\,T_H Q_{ch} + \left(1 - \eta_{HR}\right) C_p \Delta T} \tag{4}$$

where T_H is the high temperature of the TREC system, η_{HR} is the efficiency of heat recuperation, and C_p is the heat capacity.[12] The heat-to-electricity conversion efficiency has an inverse relationship with the heat capacity, determining the amount of heat energy required to increase the system temperature. The DSC data (Figures S3,S4, Supporting Information) indicate a significantly lower heat capacity for O/Cu-1.0 (0.285 mWh g^{-1} K^{-1}) compared to O/Cu-1.3 (0.332 mWh g^{-1} K^{-1}) and O/Cu-1.5 (0.389 mWh g^{-1} K^{-1}). As a consequence, O/Cu-1.0 is expected to possess a higher heat-to-electricity conversion efficiency than O/Cu-1.5 due to its smaller heat capacity and a larger amount of harvested work. When the heat recuperation system is not operational ($\eta_{HR} = 0$), the first-cycle efficiencies for O/Cu-1.0 are 3.66% (ΔT = 50 °C), 3.80% (ΔT = 40 °C), and 2.55% (ΔT = 30 °C). For O/Cu-1.5, these efficiencies are 2.71%, 2.47%, and 1.21%, respectively (Figure 3d). The amount of harvested work decreases with increasing current density, resulting in a larger overpotential. Hence, the TREC cells with a current density of 1 C (60 mA g^{-1}, Figure 3e) and 2 C (120 mA g^{-1}, Figure 3f) provide smaller amounts of harvested work than those with a current density of 0.5 C (Figure 3c). The work is not harvested when ΔT is below 40 °C for 1 C or below 50 °C for 2 C because the temperature difference is insufficient to overcome the larger overpotential. These results indicate that a sufficiently high-temperature coefficient is necessary for harvesting additional work under high current density. The average harvested work was 1.89 J K^{-1} (ΔT = 50 °C at 1 C), 1.38 J K^{-1} (ΔT = 40 °C at 1 C), and 0.45 J K^{-1} (ΔT = 50 °C at 2 C) for O/Cu-1.5 and 3.01, 2.07, and 0.68 J K^{-1} for O/Cu-1.0 respectively. In the absence of heat recuperation, the first-cycle efficiencies for O/Cu-1.5 are 1.86% (ΔT = 50 °C at 1 C), 1.50% (ΔT = 40 °C at 1 C), and 0.68% (ΔT = 50 °C at 2 C). For O/Cu-1.0, these efficiencies are 3.53%, 2.97%, and 1.31%, respectively, as shown in Figure 3g,h. Thus, the electrode material in the TREC cell with a higher temperature coefficient can harvest more work with higher conversion efficiency. In addition, the heat-to-electricity efficiency tends to increase with a heat-recuperation system (η_{HR} = 50 in Figure 3d,g,h), which reuses additional waste-heat energy generated by operating the TREC system.[21,12] The detailed values for absolute and relative efficiencies are provided in Tables S3,S4 (Supporting Information). Therefore, we can validate the potential for further enhancing the efficiency of TREC through the design of a heat-recuperation system.

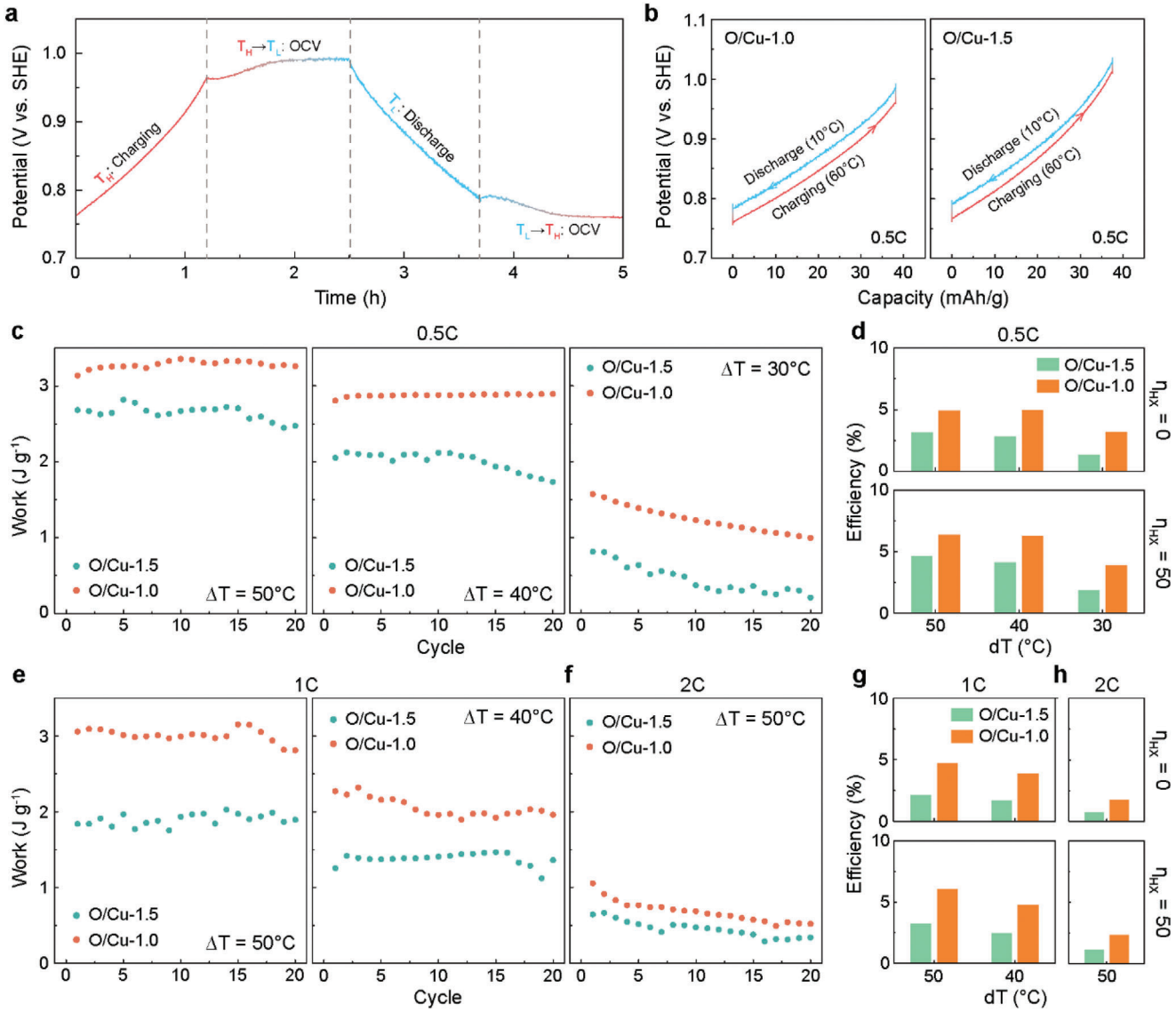

Figure 3. TREC half-cell cycles. a) Voltage profile of 1 cycle of TREC half-cell system as a function of time. b) Closed loop TREC cycle for O/Cu-1.5 and O/Cu-1.0. c) Amount of harvested work at different temperatures (50 °C (left), 40 °C (middle), and 30 °C (right)) with a current density of 0.5 C. d) The corresponding efficiency of the TREC under the same conditions as (c). e) Amount of harvested work at a current density of 1 C. The temperature differences are 50 °C (left) and 40 °C (right). f) Amount of harvested work at the current density of 2 C. The temperature difference is 50 °C. g) Efficiency of the TREC under the same conditions as (e). h) Efficiency of TREC under the same conditions as (f). The efficiencies in (d), (g), and (h) were calculated for 0% and 50% heat recuperation (η_{HX}).

2.3. Effect of Amount of Water Molecules on Stretching Modes of Cyanide Ligands

Raman and Fourier-transform infrared (FT-IR) spectroscopy are suitable tools for identifying the molecular vibrational modes for comparison of the degree of bonding covalency in the CuHCFe structure depending on the number of water molecules. Previous research has identified three types of vibration modes in CuHCFe: E_g, A_{1g}, and T_{1u},[16] with E_g and A_{1g} being Raman active and T_{1u} being IR active. For T_{1u}, the bonding on the z-axis moves toward the $+z$-direction and those on the x- and y-axis move toward the $-z$-direction, which is not directly related to cyanide ligand covalency.[22] The peak position of T_{1u}[16] with Fe(III) appears near 2173 cm^{-1} and that with Fe(II) near 2097 cm^{-1}. As shown in Figure S5 (Supporting Information), the two peaks are shown for the pristine and SOC 100% states in FT-IR spectra of O/Cu-1.5, O/Cu-1.3, and O/Cu-1.0. The 2097 cm^{-1} peaks in both the pristine and SOC 100% states correspond to the partially reduced state of Fe(III) to Fe(II). The intensity and position of T_{1u} remained unchanged during the cycle for all the samples, indicating that the vibration of T_{1u} is unaffected by the amounts of water molecules and cyanide-ligand covalency.

In contrast, the Raman peaks exhibit noticeable variations among the samples and the states (**Figure 4**a). The Raman spectra of the pristine samples demonstrate that the peak intensity

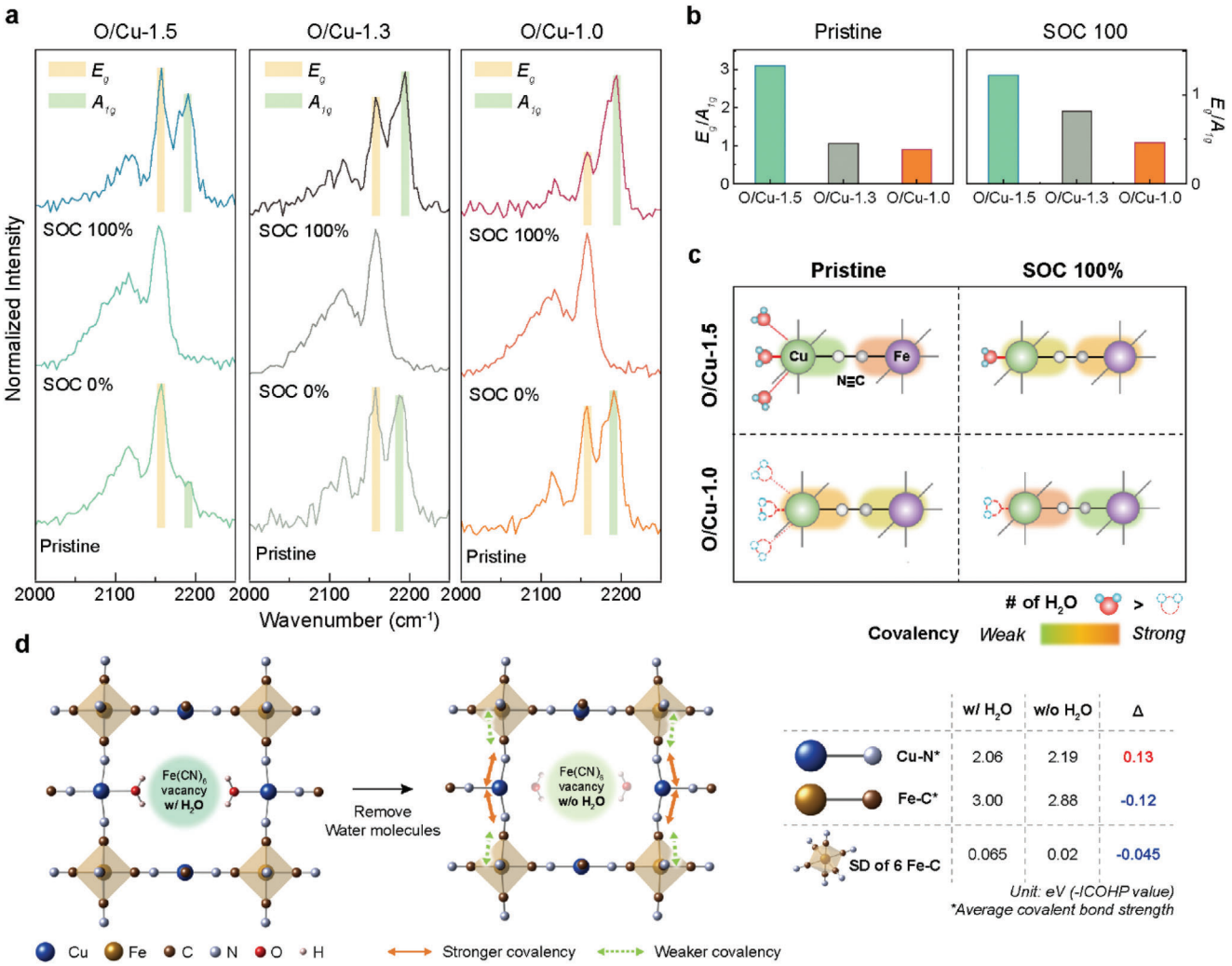

Figure 4. Raman spectra and schematic illustrating the change in bonding covalency by the presence of water molecules. a) Raman spectra of O/Cu-1.5, O/Cu-1.3, and O/Cu1.0 in pristine, SOC 0%, and SOC 100% states. b) Ratio of E_g to A_{1g} for O/Cu-1.5, O/Cu-1.3, and O/Cu-1.0 in the pristine and SOC 100% states. c) Schematic showing the effect of water molecules on Cu—N and Fe—C bonding covalency. d) Effect of removal of water molecules on the CuHCFe structure and covalency variation (-ICOHP/eV). The average -ICOHP values of Cu—N and Fe—C bonds and the SD of -ICOHP values of 6 Fe—C bonds are presented.

of E_g increases whereas that of A_{1g} decreases with the increasing amount of water molecules, resulting in the highest E_g and lowest A_{1g} peak intensity for O/Cu-1.5. Regardless of the sample type, interstitial water molecules are easily moveable with intercalated sodium ions during electrochemical reactions.[23,24] Consequently, after the extraction of sodium ions at SOC 100%, the peak intensity of E_g decreases whereas that of A_{1g} increases due to the absence of some interstitial water molecules. In contrast, coordinated water remains stationary with sodium ions, thereby maintaining its inherent properties and resulting in a relatively higher peak intensity of E_g in O/Cu-1.5 and A_{1g} in O/Cu-1.0, as shown in Figure 4b. The ratio of E_g to A_{1g} was substantially higher in O/Cu-1.5 and decreased in the order of O/Cu-1.3 > O/Cu-1.0. At SOC 100%, the overall ratio decreased but the same tendency remained. Unlike for the pristine and SOC 100% states, the Raman spectra of the SOC 0% state were nearly identical for each sample. This finding might be attributed to intercalated sodium ions, which can dominate the temperature coefficient value, as indicated in Figure 2e. The insertion of cations significantly changes the entire CuHCFe system, possibly overwhelming the local vibration of the structure.

As shown in Figure 1d, in the E_g mode, cyanide ligands on the z-axis elongate in opposite directions, whereas those on the x- and y-axes contract along their respective axes. In contrast, in the A_{1g} mode, cyanide ligands on the x- and y-axis elongate along the axis.[22] Consequently, the bonding should be easily contracted for a strong E_g intensity, indicating that the Cu—N bonding possesses relatively weak covalency and that the Fe—C bonding possesses relatively strong covalency. Unlike E_g, A_{1g} requires strong covalency of Cu—N bonding and weak covalency of Fe—C bonding for easier elongation. Therefore, we suggest that the degree of covalency greatly depends on the amounts of water molecules in the CuHCFe structure, as shown in Figure 4c, which induces different preferred vibration modes. As the amount of water molecules

decreases, the Cu—N bond covalency becomes stronger, whereas the Fe—C bond covalency decreases.

To investigate the effect of water molecules on the local environment and the bonding nature of Cu—N and Fe—C bonds surrounding the $Fe(CN)_6$ vacancy, we calculated the integrated crystal orbital Hamilton population (-ICOHP) values.[25–27] The CuHCFe structures with and without water molecules were prepared and fully relaxed using generalized gradient approximation (GGA) + U (see Computational Details for further information), and one layer of relaxed PBA structures projected along the *y*-direction is shown in Figure 4d (left). Upon the removal of water molecules, the contraction of Cu—N bonds and expansion of Fe—C bonds were observed, which is consistent with our prediction (Figure 4c). An upward trend in the average -ICOHP value for Cu—N bonds around the vacancy was observed, indicating increased bond covalency. In contrast, the downward trend in -ICOHP values for Fe—C bonds indicates reduced bond covalency (Cu—N* and Fe—C* in Figure 4d). Further examination reveals that the strength of these Fe—C bonds decreases, causing their -ICOHP values to become notably similar to those of neighboring Fe—C bonds and resulting in a more symmetric bond-strength distribution. To quantify this observation, we analyzed the standard deviation (SD) of -ICOHP values for Fe—C bonds in FeC_6 octahedra (SD of 6 Fe—C in Figure 4d), which exhibited a decrease in the structure without water molecules. As previously mentioned, the Raman A_{1g} peak with lower water content corresponds to simultaneous contraction and stretching in six directions centered on the metal ion. Consequently, the reduction in the standard deviation of Fe—C bond values supports the observed trend in the Raman A_{1g} peak,[17] further emphasizing the effect of water molecules on the electronic structure and vibrational mode of the system.

The Raman spectra and computational simulation results indicate that a deficiency of water molecules in CuHCFe enhances the Cu—N bond covalency while decreasing the Fe—C bond covalency, resulting in the strong A_{1g} vibration mode. Because the A_{1g} mode appears at larger wavenumbers than the E_g mode (Figure 1d), A_{1g} can infer higher vibrational energy with a relatively aggressive motion,[28,29] inducing significant changes in structural vibration entropy. Consequently, our result validates that CuHCFe with a smaller amount of water molecules possesses a larger temperature coefficient.

2.4. TREC Full-Cell Demonstration of O/Cu-x and Co-gr

Taking advantage of the above-designed entropy term, we demonstrate the TREC full-cell with a cathode of O/Cu-x and an anode of cobalt hexacyanoferrate-green (CoHCFe-green, Co-gr) that undergoes a two-step redox reaction: $Co^{II}[Fe^{II}(CN)_6] \leftrightarrow Co^{III}[Fe^{II}(CN)_6] \leftrightarrow Co^{III}[Fe^{III}(CN)_6]$.[30] As a result of different phonon entropy changes according to lattice parameter changes, Co-gr exhibits a positive temperature coefficient for the redox reaction of $Co^{II/III}$ and a negative temperature coefficient for the redox reaction of $Fe^{II/III}$.[10] Based on **Figure 5**a, Co-gr has a positive temperature coefficient of 0.370 mV K^{-1} at SOC 10% and 0.154 mV K^{-1} at SOC 30%. The temperature coefficient of the full cell is the difference between the temperature coefficient of the cathode and anode materials ($\alpha_{cell} = \alpha_{cathode} - \alpha_{anode}$, where α_{cell}, $\alpha_{cathode}$, and α_{anode} are the temperature coefficients of the cell, cathode, and anode, respectively.). Therefore, we can design a TREC cycle by using electrode materials with the opposite direction of temperature coefficients, resulting in an ideal system with a higher temperature coefficient for the cell. Figure 5b demonstrates that the voltage changes of Co-gr and CuHCFe occur in the opposite direction. At a higher temperature (T_H), the voltage of the cathode with CuHCFe decreases, and that of the anode with Co-gr increases (the full-cell voltage is E_H), and the voltages change in the opposite direction at a lower temperature (the full-cell voltage is E_L). Therefore, when the cell is charged at a higher temperature and discharged at a lower temperature, the heat energy is effectively transformed into electrochemical energy as the amount of $(E_L - E_H) \times$ capacity. As a result of the TREC full-cell design, the Cu-$1.5_{cathode}$–Co-gr_{anode} system exhibits a temperature coefficient of −0.905 mV K^{-1}, whereas the O/Cu-$1.0_{cathode}$–Co-gr_{anode} system exhibits a temperature coefficient −1.017 mV K^{-1}, as shown in Figure 5c. The activation process at the initial cycle is caused by the relatively high mass loading of Co-gr to use the SOC range of SOC 15% to SOC 25% (Figure 5d). After activation, the maximum amount of harvested work is 3.45 J g^{-1} for the O/Cu-$1.0_{cathode}$–Co-gr_{anode} system and 3.04 J g^{-1} for the Cu-$1.5_{cathode}$–Co-gr_{anode} system. However, the performance of the TREC full-cell system degrades more rapidly than that of the TREC half-cell system due to the poor thermal stability of Co-gr[31] (Figure S6, Supporting Information). However, the cyclability of the O/Cu-x TREC half-cell system is stable for 100 cycles, indicating that the vibration modes of cyanide ligands do not change as the cycle repeats. In other words, coordinated water molecules are strongly bonded to Cu(II) during redox reactions, whereas interstitial water molecules move reversibly in and out of CuHCFe channels with sodium ions. As a consequence, the entropy changes of CuHCFe caused by water molecules are not a one-time reaction but a persistent reaction.

3. Conclusion

In conclusion, we present the design of a TREC system that achieves high efficiency by controlling the structural vibrational entropy change. The findings validate that the structural vibration mode, influenced by the number of water molecules in the structure, plays a significant role in determining the degree of structural vibrational entropy change. Through a combination of Raman spectra analysis and computational simulations, we establish that coordinated and interstitial water molecules have the ability to modulate the covalency of the transition metal and cyanide ligands. In the absence of these water molecules, a stronger covalency in the Cu—N bonds and a weaker covalency in the Fe—C bonds enhance the A_{1g} vibration mode, resulting in higher structural energy and a large structural entropy change. By using the inherent characteristics, we can design a TREC system that exhibits a high heat-to-electricity conversion efficiency. By focusing on the intrinsic properties of PBAs with structural water molecules, we contribute valuable insight for the advancement of next-generation battery and self-charging systems. This work bridges the gap between scientific understanding and practical implementation.

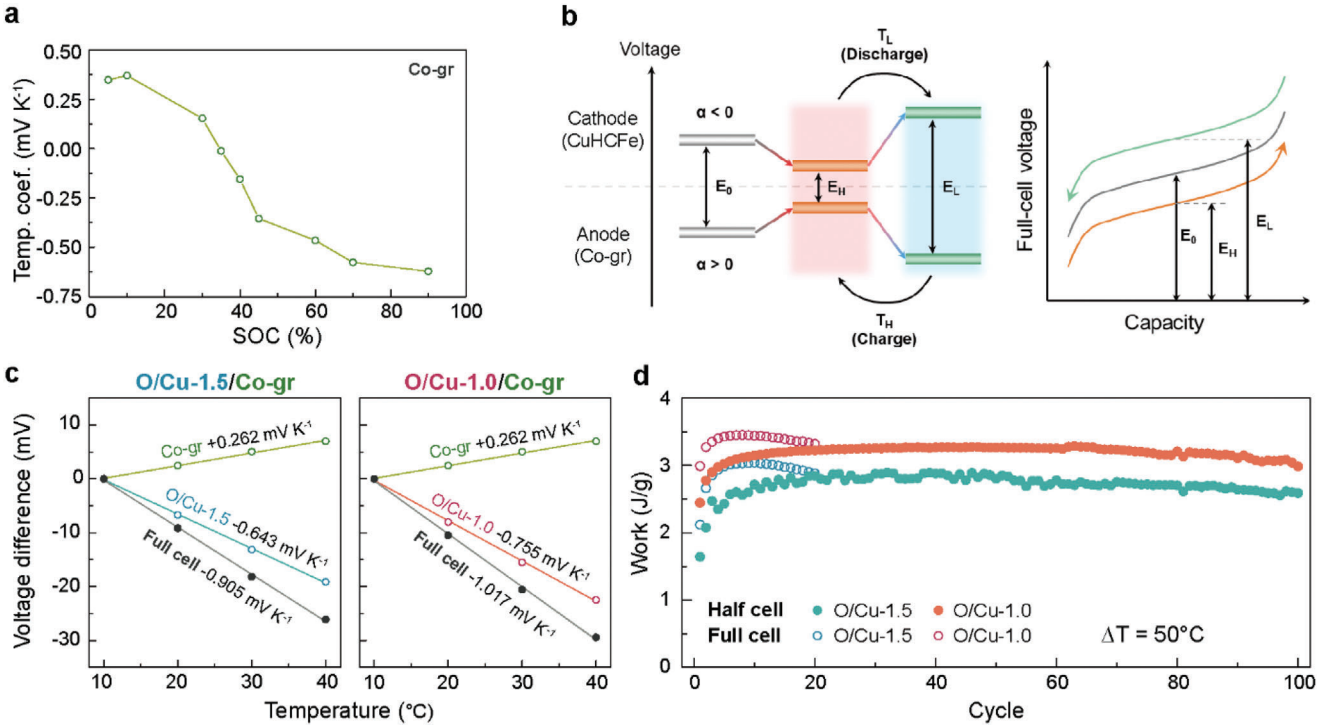

Figure 5. TREC full-cell demonstration. a) Temperature coefficient of Co-gr from SOC 5% to SOC 90%. b) Voltage changes of CuHCFe cathode and Co-gr anode (left) and full cell (right). T_L represents low temperature, T_H represents high temperature, E_L represents the full-cell voltage at low temperature, E_H represents the full-cell voltage at high temperature, and E_0 represents the full-cell voltage at normal state. c) Voltage plot of O/Cu-1.5, Co-gr, and full cell (left). Voltage plot of Cu-1.0, Co-gr, and full cell (right). d) Amount of harvested work as a result of TREC full-cell and half-cell. The low and high temperatures are 10 and 60 °C, respectively. The current density of the full cell is set at 0.5 C (30 mA g^{-1}) based on O/Cu-x.

4. Experimental Section

Synthesis of O/Cu-x: O/Cu-x was synthesized using a co-precipitation method, which was previously used to synthesize PBA materials.[32] An aqueous solution of $Cu(NO_3)_2{\bullet}3H_2O$ (0.04 M, 100 ml) and $K_3Fe(CN)_6$ (0.02 M, 100 ml) were added to deionized (DI) water (50 ml) for 1 h. After stirring for 1 h, the precipitate was aged overnight without additional stirring at room temperature. The reaction and stirring temperatures were 7 °C for O/Cu-1.5, 40 °C for O/Cu-1.3, and 90 °C for O/Cu-1.0. After the aging step, the precipitate was washed three times with DI water and once with acetonitrile. It was dried overnight under vacuum at 40 °C.

Synthesis of Co-gr: Co-gr was synthesized using a method similar to that used to prepare O/Cu-x. An aqueous solution of $Co(NO_3)_2{\bullet}6H_2O$ (0.04 M, 100 ml) and $K_4Fe(CN)_6{\bullet}3H_2O$ was added to NaCl solution (5 M, 50 ml) for 1 h at 30 °C. After stirring for 1 h at the same temperature, the precipitate was washed three times with DI water. It was dried for 15 h under vacuum at 100 °C.

Material Characterization: The chemical formula was determined by using ICP-MS for K, Na, Cu, and Fe. The amount of water in Cu-x and Co-gr was determined by TGA by heating the sample to 350 °C at 1 °C min^{-1} under N_2. The crystal structures of O/Cu-x were observed using synchrotron X-ray diffraction (XRD). The lattice parameters and space groups were confirmed with Le Bail fit using FullProf.[33]

Electrochemical Measurement: Working electrodes were prepared by mixing 80 wt.% O/Cu-x or Co-gr, 10 wt.% carbon black and 10 wt.% polyvinylidene difluoride (PVDF) binder in 1-methyl-2-pyrrolidone using a planetary mixer (ARE-310). Active material slurries were coated on carbon cloth and dried overnight under vacuum at 40 °C for O/Cu-x or for 2 h under vacuum at 90 °C for Co-gr. Counter electrodes were prepared by mixing 90 wt.% activated carbon and 10 wt.% PVDF binder in 1-methyl-2-pyrrolidone using a planetary mixer. The activated carbon slurries were coated on carbon cloth and dried overnight under vacuum at 40 °C. All the electrochemical measurements were performed in a flooded three-electrode cell with 20 ml of electrolyte. The electrolyte was 1 M aqueous $NaNO_3$ prepared by using N_2-purged DI water. An Ag/AgCl reference electrode (with saturated KCl solution) was used as the reference electrode. The electrochemical test was performed using a BioLogic VMP3 multichannel battery tester.

Computational Details: First-principles calculations were carried out using the Vienna Ab initio Simulation Package.[34] The calculations were performed using GGA with Perdew–Burke–Ernzerhof exchange-correlation functional.[35] The van der Waals correction was incorporated using Grimme's D3 method to address weak long-range interactions.[36,37] The DFT + U approach[38] was used with U values of 1 eV for Fe and 3 eV for Cu, following the same values used for CuHCFe in previous works of literature.[39,40] For the CuHCFe structures, an energy cut-off of 550 eV and 1 × 1 × 2 Γ-centered K-point grid was used. Atomic coordinates, cell volume, and cell shape were fully relaxed until the forces of each atom were below 0.05 eV $Å^{-1}$. To simulate the $Fe(CN)_6$ vacancies in the structure, a 2 × 2 × 1 supercell was constructed with the distribution of vacancies based on the research by Xianyong Wu et al.[33] To investigate the effect of the temperature on coordinated waters, AIMD simulations were conducted within the canonical ensemble using a Nosé–Hoover thermostat. To strike a balance between computational efficiency and accuracy, calculations were performed using a Γ-centered 1 × 1 × 1 k-point grid. The CuHCFe structures were initially set up with water molecules positioned close to Cu sites, which were coordinated by three or four CN groups exhibiting non-bonding behavior near the $Fe(CN)_6$ vacancy (Figure S7, Supporting Information). The simulation began at an initial temperature of 100 K, with velocities assigned based on the Boltzmann distribution. Employing a time step of 1 fs, the temperature was incrementally increased over 200 steps, eventually reaching the target temperatures (280, 313, 363, and 413 K). Subsequently, at each equilibrium temperature, structures with various water molecule configurations were attained for 2.5 ps

simulation time. Averaged pRDF curves were calculated using the pymatgen diffusion module.[41,42] The bonding information was derived from the electronic wavefunctions using a Γ-centered 2 × 2 × 4 k-point grid for CuHCFe structures. The LOBSTER (Local Orbitals Basis Suite Toward Electronic–Structure Reconstruction) code was used to calculate the Crystal Orbital Hamilton Population, which allowed for evaluating the contributions of electrons to individual bonds.[25–27]

Supporting Information

Supporting Information is available from the Wiley Online Library or from the author.

Acknowledgements

A.C. and Y.-Y.S. contributed equally to this work. This work was supported by the 2023 Research Fund (1.230040.01) of UNIST, Individual Basic Science & Engineering Research Program (RS-2023-00208929, 2023R1A2C2008242), and the National Center for Materials Research Data (2021M3A7C2089743) through the National Research Foundation (NRF) of Korea funded by the Ministry of Science and ICT (MSIT). The computational work was supported by the Supercomputing Center/Korea Institute of Science and Technology Information with supercomputing resources including technical support (KSC-2022-CRE-0343 to H.-W.L.). S.W.L. acknowledges the support by the NRF, Prime Minister's Office, Singapore under its NRF-ANR Joint Programme (grant number Award No. NRF2019-NRF-ANR052 KineHarvest). This study contained the results obtained by using the equipment of UNIST Central Research Facilities (UCRF). The HR-XRD experiments performed at Beamline 6D of the Pohang Accelerator Laboratory were supported in part by the MSIT, POSTECH, and UCRF at UNIST.

Conflict of Interest

The authors declare no competing financial interest.

Data Availability Statement

The data that support the findings of this study are available from the corresponding author upon reasonable request.

Keywords

low-grad heat harvesting, Prussian Blue analogs, structural vibration, structural vibration entropy, thermally regenerative electrochemical cycles

Received: April 5, 2023
Revised: June 22, 2023
Published online: July 26, 2023

[1] S. Chu, A. Majumdar, *Nature* **2012**, *488*, 294.
[2] F. Bonaccorso, L. Colombo, G. Yu, M. Stoller, V. Tozzini, A. C. Ferrari, R. S. Ruoff, V. Pellegrini, *Science* **2015**, *347*,1246501.
[3] M. Massetti, F. Jiao, A. J. Ferguson, D. Zhao, K. Wijeratne, A. Würger, J. L. Blackburn, X. Crispin, S. Fabiano, *Chem. Rev.* **2021**, *121*, 12465.
[4] R. A. Kishore, B. Davis, J. Greathouse, A. Hannon, D. E. Kennedy, A. Millar, D. Mittel, A. Nozariasbmarz, M. G. Kang, H. B. Kang, M. Sanghadasa, S. Priya, *Energy Environ. Sci.* **2019**, *12*, 1008.
[5] C. Geffroy, D. Lilley, P. S. Parez, R. Prasher, *Joule* **2021**, *5*, 3080.
[6] J. Duan, B. Yu, L. Huang, B. Hu, M. Xu, G. Feng, J. Zhou, *Joule* **2021**, *5*, 768.
[7] Y. Zhang, P. T. T. Phuong, E. Roake, H. Khanbareh, Y. Wang, S. Dunn, C. Bowen, *Joule* **2020**, *4*, 301.
[8] S. W. Lee, Y. Yang, H. W. Lee, H. Ghasemi, D. Kraemer, G. Chen, Y. Cui, *Nat. Commun.* **2014**, *5*, 4942.
[9] S. J. Banik, R. Akolkar, *J. Electrochem. Soc.* **2013**, *160*, D519.
[10] C. Gao, Y. Yin, L. Zheng, Y. Liu, S. Sim, Y. He, C. Zhu, Z. Liu, H. W. Lee, Q. Yuan, S. W. Lee, *Adv. Funct. Mater.* **2018**, *28*, 1803129.
[11] C. Gao, Y. Liu, B. Chen, J. Yun, E. Feng, Y. Kim, M. Kim, A. Choi, H. W. Lee, S. W. Lee, *Adv. Mater.* **2021**, *33*, 2004717.
[12] J. Jiang, H. Tian, X. He, Q. Zeng, Y. Niu, T. Zhou, Y. Yang, C. Wang, *J. Mater. Chem. A* **2019**, *7*, 23862.
[13] C. D. Wessells, R. A. Huggins, Y. Cui, *Nat. Commun.* **2011**, *2*, 1563.
[14] P. Bhatt, S. S. Meena, M. D. Mukadam, B. P. Mandal, A. K. Chauhan, S. M. Yusuf, *New J. Chem.* **2018**, *42*, 4567.
[15] S. F. A. Kettle, G. L. Aschero, E. Diana, R. Rossetti, P. L. Stanghellini, *Inorg. Chem.* **2006**, *45*, 4928.
[16] J. Mink, A. Stirling, D. O. Ojwang, G. Svensson, J. Mihály, C. Németh, M. Drees, L. Hajba, *Appl. Spectrosc. Rev.* **2019**, *54*, 369.
[17] S. F. A. Kettle, E. Diana, E. M. C. Marchese, E. Boccaleri, P. L. Stanghellini, *J. Raman Spectrosc.* **2011**, *42*, 2006.
[18] W. Wei, W. Li, K. T. Butler, G. Feng, C. J. Howard, M. A. Carpenter, P. Lu, A. Walsh, A. K. Cheetham, *Angew. Chem.* **2018**, *130*, 9070.
[19] W. J. Li, C. Han, G. Cheng, S. L. Chou, H. K. Liu, S. X. Dou, *Small* **2019**, *15*, 1900470.
[20] M. Pasta, C. D. Wessells, N. Liu, J. Nelson, M. T. McDowell, R. A. Huggins, M. F. Toney, Y. Cui, *Nat. Commun.* **2014**, *5*, 4007.
[21] X. Qian, J. Shin, Y. Tu, J. H. Zhang, G. Chen, *Phys. Chem. Chem. Phys.* **2021**, *23*, 22501.
[22] K. Eddahaoui, S. Benmokhtar, B. Manoun, S. Belaaouad, P. Lazor, *Spectrochim. Acta, Part A* **2012**, *99*, 81.
[23] C. D. Wessells, S. V. Peddada, R. A. Huggins, Y. Cui, *Nano Lett.* **2011**, *11*, 5421.
[24] Y. Mizuno, M. Okubo, E. Hosono, T. Kudo, H. Zhou, K. Oh-Ishi, *J. Phys. Chem. C* **2013**, *117*, 10877.
[25] V. L. Deringer, A. L. Tchougréeff, R. Dronskowski, *J. Phys. Chem. A* **2011**, *115*, 5461.
[26] R. Dronskowski, P. E. Blochl, *J. Phys. Chem.* **1993**, *97*, 8617.
[27] S. Maintz, V. L. Deringer, A. L. Tchougréeff, R. Dronskowski, *J. Comput. Chem.* **2013**, *34*, 2557.
[28] H. Kuramochi, T. Tahara, *J. Am. Chem. Soc.* **2021**, *143*, 9699.
[29] S. Mosca, C. Conti, N. Stone, P. Matousek, *Nat. Rev. Methods Primers* **2021**, *1*, 21.
[30] L. Ma, S. Chen, C. Long, X. Li, Y. Zhao, Z. Liu, Z. Huang, B. Dong, J. A. Zapien, C. Zhi, *Adv. Energy Mater.* **2019**, *9*, 1902446.
[31] X. Wu, C. Wu, C. Wei, L. Hu, J. Qian, Y. Cao, X. Ai, J. Wang, H. Yang, *ACS Appl. Mater. Interfaces* **2016**, *8*, 5393.
[32] H. W. Lee, M. Pasta, R. Y. Wang, R. Ruffo, Y. Cui, *Faraday Discuss.* **2014**, *176*, 69.
[33] X. Wu, J. J. Hong, W. Shin, L. Ma, T. Liu, X. Bi, Y. Yuan, Y. Qi, T. W. Surta, W. Huang, J. Neuefeind, T. Wu, P. A. Greaney, J. Lu, X. Ji, *Nat. Energy* **2019**, *4*, 123.
[34] G. Kresse, J. Furthmü, *Phys. Rev. Lett.* **1996**, *77*, 3865.
[35] J. P. Perdew, K. Burke, M. Ernzerhof, *J. Chem. Phys.* **1996**, *132*, 154104.
[36] S. Grimme, J. Antony, S. Ehrlich, H. Krieg, *J. Chem. Phys.* **2010**, *132*, 154104.

[37] S. Grimme, S. Ehrlich, L. Goerigk, *J. Comput. Chem.* **2011**, *32*, 1456.
[38] S. L. Dudarev, G. A. Botton, S. Y. Savrasov, C. J. Humphreys, A. P. Sutton, *Phys. Rev. B* **1998**, *57*, 1505.
[39] E. Targholi, S. M. Mousavi-Khoshdel, M. Rahmanifara, M. Z. A. Yahya, *Chem. Phys. Lett.* **2017**, *687*, 244.
[40] X. Wang, S. Pandey, M. Fullarton, S. R. Phillpot, *J. Phys. Chem. C* **2021**, *125*, 24273.
[41] Z. Deng, Z. Zhu, I. H. Chu, S. P. Ong, *Chem. Mater.* **2017**, *29*, 281.
[42] S. P. Ong, W. D. Richards, A. Jain, G. Hautier, M. Kocher, S. Cholia, D. Gunter, V. L. Chevrier, K. A. Persson, G. Ceder, *Comput. Mater. Sci.* **2013**, *68*, 314.